ARTICLES
PUBLISHED ONLINE: 28 JULY 2013 | DOI: 10.1038/NPHOTON.2013.190
nature photonics

Compact spectrometer based on a disordered photonic chip

Brandon Redding, Seng Fatt Liew, Raktim Sarma and Hui Cao*

Light scattering in disordered media has been studied extensively due to its prevalence in natural and artificial systems. In photonics most of the research has focused on understanding and mitigating the effects of scattering, which are often detrimental. For certain applications, however, intentionally introducing disorder can actually improve device performance, as in photovoltaics. Here, we demonstrate a spectrometer based on multiple light scattering in a silicon-on-insulator chip featuring a random structure. The probe signal diffuses through the chip generating wavelength-dependent speckle patterns, which are detected and used to recover the input spectrum after calibration. A spectral resolution of 0.75 nm at a wavelength of 1,500 nm in a 25-μm-radius structure is achieved. Such a compact, high-resolution spectrometer is well suited for lab-on-a-chip spectroscopy applications.

Spectrometers are widely used tools in chemical and biological sensing, materials analysis and light source characterization. The development of a high-resolution on-chip spectrometer could enable compact, low-cost spectroscopy for portable sensing as well as increasing lab-on-a-chip functionality. However, the spectral resolution of grating-based spectrometers scales with the optical path length, which translates to the linear dimension or footprint of the system. As a result, on-chip spectrometers based on curved gratings (Echelle)[1,2] and arrayed waveguide gratings[2–6] require relatively large footprints (~1–2 cm). This limitation inspired researchers to develop a number of alternative spectrometer designs. On-chip digital planar holography[7–9] has been shown to provide high resolution, but its sensitivity is limited. A dispersive photonic-crystal lattice[10], operating in the slow light regime, combines high resolution with small footprint; however, it has only been applied to the detection of individual spectral lines. Resonant devices such as microrings[11–13], microdoughnuts[14] and photonic-crystal defect cavities[15] make the effective interaction length much longer than the physical dimension of the device, thus providing high resolution in a small footprint. Unfortunately, these devices are particularly sensitive to fabrication errors.

In addition to these carefully designed systems, disorder and scattering have also been explored for spectroscopy applications. Xu *et al.* used the spatio-spectral transmission patterns of disordered photonic crystals to construct multimodal spectrometers[16]. Kohlgraf-Owens and Dogariu showed that random scattering materials have sufficient diversity in spectral transmission to allow for precise measurements of the spectrally dependent polarization state of an optical field[17]. The working principle of random spectrometers is that the speckle pattern formed by transmitted light through a disordered system provides a sort of fingerprint, uniquely identifying the wavelength of the probe signal. In practice, the wavelength-dependent speckle patterns are measured and stored in a transmission matrix, which describes the spectral-to-spatial mapping of the spectrometer. After calibrating the transmission matrix, an arbitrary input spectrum can be reconstructed from its speckle pattern. This approach has also been applied to build spectrometers with an array of Bragg fibres[18], or a single multimode fibre[19,20]. The advantage of utilizing multiple scattering in a disordered medium is that it folds the optical paths, making the effective path length longer than the linear dimension of the system. For instance, the effective optical path length in a scattering medium characterized by transport mean free path l_t and length L scales as l_t/L^2 in the diffusive regime[21]. As a result, a small shift in the input wavelength will cause a significant change in the transmitted speckle pattern. In other words, multiple scattering enhances the spectral decorrelation of speckle patterns. The spectral resolution, which is determined by the spectral correlation width of the transmitted speckle, therefore scales as l_t/L^2. Stronger scattering reduces l_t and enhances the spectral resolution. The $1/L^2$ scaling of the resolution with L enables fine spectral resolution with a limited footprint. This enhancement occurs at all frequencies, unlike the resonant cavities, which enhance the optical path length only at discrete frequencies. However, the total transmission through a diffusive system is $\sim l_t/L$. When L is much larger than l_t, most of the input signal is reflected instead of transmitted. This loss will limit the spectrometer sensitivity.

In this work, we use multiple scattering in an on-chip random structure to build a compact spectrometer. The increased optical path length enabled fine spectral resolution in a small footprint. Furthermore, the control afforded by fabricating the scattering structure on-chip allowed us to mitigate the high insertion loss normally associated with multiple scattering. By surrounding the random structure with a full-bandgap photonic-crystal boundary, we efficiently channelled the diffusive light through the disordered medium to the detectors. We also tailored the scattering properties of the random system, which consisted of precisely positioned air cylinders etched into a silicon membrane. By introducing structural correlations to the disordered medium, we engineered the spatial Fourier spectra to reduce the out-of-plane scattering loss.

Random spectrometer design and characterization

We designed and fabricated the random spectrometer in a silicon-on-insulator (SOI) wafer. As shown in the scanning electron microscope (SEM) images in Fig. 1a, the two-dimensional scattering structure is a random array of air holes etched into the silicon layer. A ridge waveguide delivers the probe light to the random array, where light is scattered by the air holes and begins diffusing in all directions. The signal reaching the other end of the random structure is then detected. To maximize the number of detectors

Department of Applied Physics, Yale University, New Haven, Connecticut 06520, USA. *e-mail: hui.cao@yale.edu

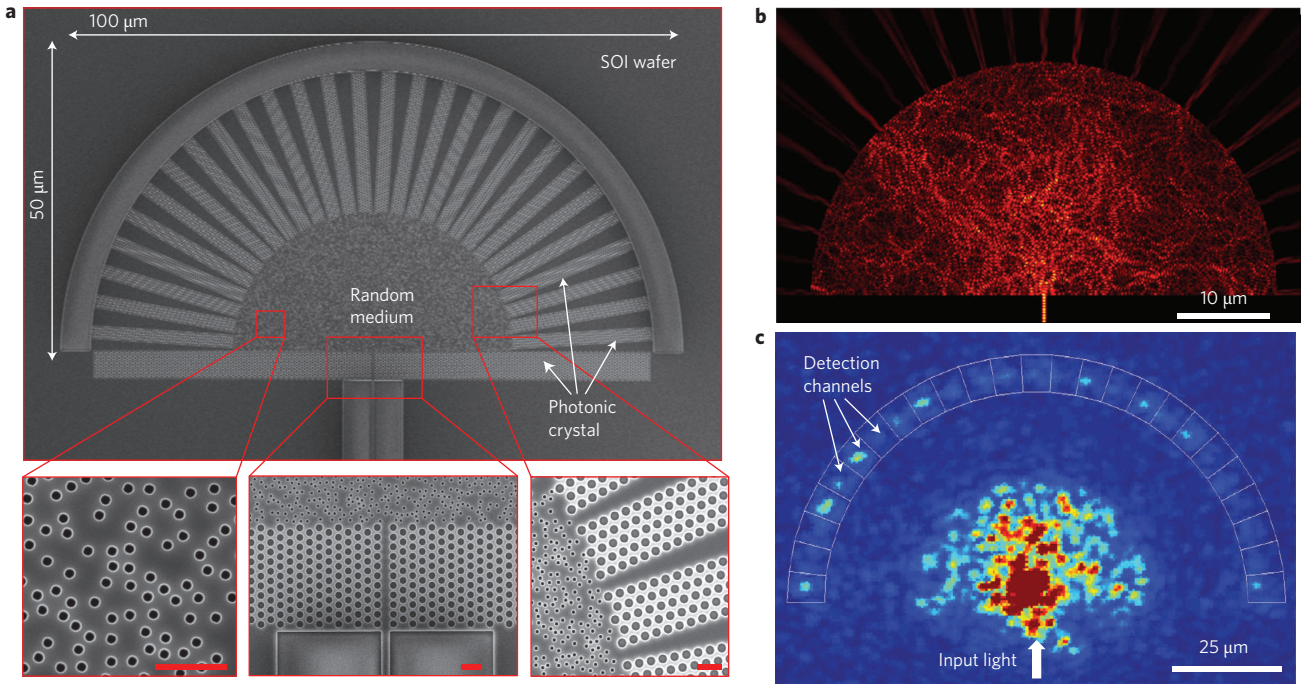

Figure 1 | A chip-based spectrometer based on multiple scattering in a disordered photonic structure. a, SEM image of the fabricated spectrometer. The dispersive element is a semicircular array of randomly positioned air holes, surrounded by a photonic-crystal lattice. The probe signal is coupled to the random structure via a defect waveguide at the bottom of the semicircle. The light then diffuses through the random array via multiple scattering and eventually reaches the 25 defect waveguides around the circumference of the semicircle. These tapered waveguides will couple the signals to the detectors (not integrated). The distribution of intensities over the detectors is used to identify the input spectrum. The photonic-crystal boundary, which has a full bandgap in two dimensions, confines the probe light in the random structure and channels it efficiently into the defect waveguides. The insets in the bottom row are magnified images, and the scale bars indicate 1 μm. **b**, Numerical simulation of TE polarized light at $\lambda = 1{,}500$ nm diffusing through the random structure. The amplitude of the H_z field shown here is calculated by the FDFD method. **c**, Experimental near-infrared optical image of the random spectrometer with a probe signal at $\lambda = 1{,}500$ nm. The white boxes, labelled 'Detection channels', mark the positions of detectors at the end of 25 defect waveguides. To avoid the complexity of integrating the detectors, we estimated the intensity coupled into each output waveguide from the integrated intensity of scattered light within each white box. The out-of-plane scattering is caused by the semicircular groove, shown in **a**, that terminates the waveguides at the location of the detectors.

and ensure that the physical distance from the input end to each detector is constant, we patterned the air holes in a semicircle. The probe signal enters from the centre of the semicircle, and diffuses outward until reaching the edge of the circle. The intensity distribution along the edge of the semicircle is used as the 'fingerprint' to uniquely identify the input spectrum. To eliminate the loss due to light escaping from the base (straight segment) of the semicircle, we placed a photonic-crystal layer (periodic array of air holes) with a full bandgap along the base. A row of holes was removed to create a defect waveguide for the input light. A similar photonic crystal boundary and defect waveguides were introduced along the circumference of the semicircle. The multiply scattered light that reaches these waveguides is channelled to the detectors. The light that hits the photonic-crystal layer between the waveguides is reflected back to the random structure and goes through further scattering until arriving at one of the defect waveguides. The output waveguides were separated by five rows of the triangular lattice of air holes to minimize their coupling, and the width of each waveguide was tapered to match the size of the detector at the end. To avoid the complexity of integrating detectors in the proof-of-concept demonstration, we terminated the output waveguides with a semicircular ridge, which scatters light out of the plane. The intensity of scattered light is proportional to that collected by each waveguide, and a microscope objective images the scattered light from above to a camera. A representative image of the scattered optical signal is shown in Fig. 1c. The input light was provided by a laser operating at $\lambda = 1{,}500$ nm. The intensity of light coupled to each output waveguide was extracted by integrating the scattered intensity measured on the camera from each detector region, as outlined by the white lines in Fig. 1c. We patterned the random spectrometer by electron-beam lithography and etching in an inductively coupled plasma reactive ion etcher (see Methods). The scattering strength was controlled by the size and density of the air holes. To model the random spectrometer, we performed numerical simulations using a finite-difference frequency-domain (FDFD) method. Figure 1b shows the H_z field amplitude of transverse electric (TE) polarized light diffusing through the semicircular random structure and coupling to the output waveguides.

The spectral resolution of the random spectrometer depends on the change in wavelength required to generate an uncorrelated intensity distribution on the detectors. It can be quantified by the spectral correlation function of the intensity on the detector plane as: $C(\Delta\lambda, x) = \langle I(\lambda, x)I(\lambda + \Delta\lambda, x)\rangle / [\langle I(\lambda, x)\rangle\langle I(\lambda + \Delta\lambda, x)\rangle] - 1$, where $I(\lambda, x)$ is the intensity recorded by detector x for input wavelength λ, and $\langle \cdots \rangle$ represents the average over λ. We measured $I(\lambda, x)$ by recording images such as the one shown in Fig. 1c as a function of probe wavelength. The spectral correlation function was then computed and averaged over all detectors, as shown in Fig. 2a for a random spectrometer with a radius of 25 μm. C is normalized to 1 at $\Delta\lambda = 0$, and its half-width at half-maximum, $\delta\lambda$, is 0.6 nm, meaning that a wavelength shift of 0.6 nm is sufficient to reduce the degree of correlation of the speckle pattern to 0.5. $\delta\lambda$ provides an estimate of the spectral resolution, because it is impossible to resolve two wavelengths with highly correlated speckle patterns.

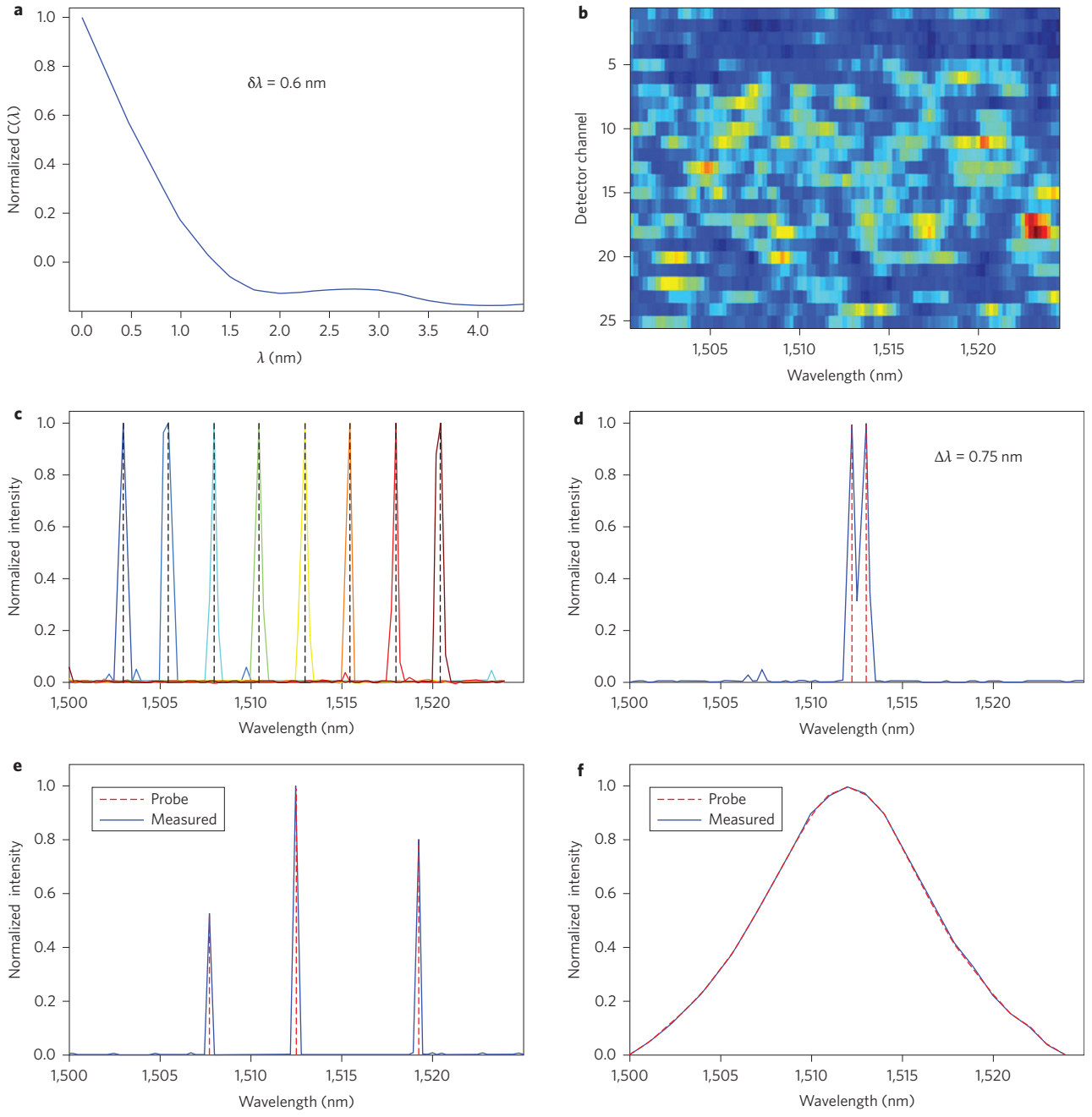

Figure 2 | Spectral calibration and testing of the random spectrometer. a, The spectral correlation function of light intensities averaged over all detection channels of a 25-μm-radius spectrometer. The half-width at half-maximum is 0.6 nm, meaning a wavelength shift of 0.6 nm reduces the degree of spectral correlation to half. **b**, The transmission matrix stores the measured intensity distribution on the detection channels as a function of the input wavelength. The matrix was calibrated by recording images such as the one in Fig. 1c for each spectral channel with a wavelength-tunable laser source. **c**, Reconstructed spectra for a series of narrow spectral lines across the 25 nm bandwidth. The black dotted lines mark the centre wavelength of each probe line. The width of each reconstructed line is less than 0.5 nm, and the average signal-to-noise ratio is over 1,000. **d**, Reconstructed spectrum (blue line) of two narrow spectral lines separated by 0.75 nm. The red dotted lines mark the centre wavelengths of the probe lines. **e**, Reconstructed spectrum for multiple spectral lines with varying amplitude. The red dotted lines mark the position and amplitude of the probe spectrum. **f**, Reconstructed spectrum for a continuous, broadband probe spectrum.

The actual resolution also depends on the reconstruction algorithm and the experimental noise of the measurements. To estimate the experimental noise, we repeatedly measured the speckle pattern generated at a fixed input wavelength and monitored the change in the speckle pattern. The coefficient of variation of the speckle patterns was ~0.04.

To use the random system as a spectrometer, we first calibrated the spectral-to-spatial mapping by recording the wavelength-dependent intensity distributions on the detectors. This calibration was stored in a transmission matrix T, relating the discretized spectral channels of the input, S, to the intensity measured by different detectors, I, as $I = TS$ (ref. 20). Each column in T describes the intensity distribution on the detectors produced by input light in one spectral channel. The number of independent spectral channels (separated by $2\delta\lambda$) that can be measured simultaneously is limited by the number of independent spatial channels (separated by the

spatial correlation length of the speckle). In our implementation, the output waveguides were separated by five rows of the photonic-crystal lattice (~2,300 nm) to avoid coupling between neighbouring waveguides and to assure that the signal reaching each detector was uncorrelated. With M detectors, the bandwidth is limited to $2M\delta\lambda$. However, unlike a grating-based spectrometer, there is no requirement that the spectral channels in a random spectrometer be contiguous. If the probe signals are confined to separated spectral regions, the transmission matrix only needs to be calibrated for these spectral regions, providing a more efficient use of the spectral channels allowed by the number of detectors. For a 25-μm-radius spectrometer with 25 independent detectors, we chose a bandwidth of 25 nm (from $\lambda = 1{,}500$ nm to 1,525 nm). The spectral channel spacing was selected to be 0.25 nm, which is less than $\delta\lambda$ to test the limit of the spectrometer resolution. Calibration was then conducted by setting a tunable laser to the centre wavelength of each spectral channel and recording the intensity distribution, thereby measuring T one column at a time. A representative transmission matrix is shown in Fig. 2b.

After calibration, an arbitrary probe spectrum can be reconstructed by measuring the intensity of light reaching the detectors (I) and multiplying it by the inverse of the transmission matrix: $S = T^{-1}I$. In practice, the matrix inversion process is susceptible to experimental noise. To improve the accuracy of the spectral reconstruction, we combined the matrix inversion process with a nonlinear optimization procedure to find the input spectra S that minimizes $\|I - TS\|^2$ (ref. 20)(Supplementary Section S1). Using this combination of matrix inversion and nonlinear optimization, we tested the ability of the random spectrometer to resolve a series of narrow lines across the 25 nm bandwidth. As shown in Fig. 2c, the spectrometer accurately recovers the positions of the individual lines with an average signal-to-noise ratio of ~1,000. The linewidth is less than 0.5 nm. We then characterized the spectral resolution of the spectrometer by testing its ability to resolve two closely spaced spectral lines. To synthesize the probe spectrum, we added the intensity recorded separately on the detectors by the two spectral lines, $I_{\text{probe}} = I_{\lambda 1} + I_{\lambda 2}$, because light at different wavelengths does not interfere. As shown in Fig. 2d, two lines separated by merely 0.75 nm are clearly resolved. This confirms that multiple scattering in a disordered medium enables sub-nanometre spectral resolution with a 25 μm × 50 μm footprint.

In addition to narrow spectral lines, the random spectrometer can also accurately measure continuous broadband spectra. For a broad spectrum the speckle contrast is reduced because the speckle patterns generated by different wavelengths sum in intensity. If the speckle contrast approaches the noise level of the measurement, the spectrum reconstruction would suffer. However, the speckle contrast scales as $M^{-0.5}$, where M is the number of uncorrelated speckle patterns. In the random spectrometer, the number of uncorrelated speckle patterns is determined by the number of independent spectral channels, which is limited to the number of independent spatial channels or detectors. In our implementation shown in Fig. 1, there are 25 detectors, so M is limited to 25 and the minimum speckle contrast is 0.2, which is much greater than the coefficient of variation of the experimental measurements of ~0.04. Accordingly, the random spectrometer is able to accurately reconstruct continuous broadband spectra up to the calibrated 25 nm bandwidth. To confirm this, we reconstructed arbitrary spectra including multiple narrow lines with varying amplitude and continuous broadband spectra, as shown in Fig. 2e,f (see Supplementary Section S2 for more details).

Characteristics of a random spectrometer

We also modelled the thermal stability of the random spectrometer, as detailed in Supplementary Section S4. Up to a temperature change of ±4 K, the input spectra can still be accurately reconstructed. The above calibration and testing were carried out with TE polarized light (electric field parallel to the silicon layer). The same random structure can also function as a spectrometer for transverse magnetic (TM) polarized light (electric field perpendicular to the silicon layer), as long as the transmission matrix for the TM polarization, which differs from that of TE, is calibrated.

Although the grating-based on-chip spectrometer works only for a fixed spectral range because the monolithic grating cannot be rotated, the random spectrometer can operate in varying spectral regions without structural modification. This is because multiple scattering occurs in a random structure over an extremely broad range of frequency. The transport mean free path varies gradually with wavelength, so the spectral resolution is relatively constant over the wavelength range of 1,250–1,750 nm (Supplementary Section S3). A switch of the operation frequency can be done simply by changing the transmission matrix to one calibrated for the desired spectral region. However, care must be taken to ensure that no input signal outside the operation bandwidth is coupled to the spectrometer, as this would corrupt the spectrum reconstruction.

In addition to spectral resolution, bandwidth and footprint, sensitivity is another crucial metric of spectrometer performance. For the random spectrometer, a good sensitivity requires maximizing the transmission from the input waveguide through the scattering structure to the detectors. The low transmission normally associated with a disordered scattering medium is due to the open boundary: light can escape from the disordered medium in any direction. By surrounding the disordered structure with a reflecting photonic-crystal boundary, we intended to confine light in the random system, limiting the escape routes to the defect waveguides that lead to the detectors. To estimate the transmission through the disordered medium in our spectrometer, we performed two-dimensional FDFD simulations with and without the photonic-crystal boundary (Supplementary Section S5). The simulation results showed that the photonic crystal with a full bandgap dramatically improved the collection efficiency. For a semicircular random medium with a radius of 25 μm, 60% of the input light was channelled into the output waveguides, with the remaining 40% returning to the input waveguide. Without the photonic-crystal boundary, only 21% of the input reached the detectors.

The two-dimensional simulation, however, neglected loss due to out-of-plane scattering. In the near-field image of the random spectrometer (Fig. 1c), we observed a strong signal from within the random structure itself, indicating that a significant fraction of the input light was scattered out of plane before reaching the detectors. Note that the out-of-plane scattering limits not only the spectrometer sensitivity, but also the spectral resolution. For a random spectrometer with a radius of 25 μm, the experimentally measured spectral correlation width $\delta\lambda$ is 0.6 nm, while the two-dimensional simulation of the same structure, ignoring the out-of-plane scattering, gives $\delta\lambda \approx 0.3$ nm. This is because the out-of-plane leakage is larger for the longer optical paths, thereby preferentially attenuating the light going through longer paths and reducing the effective path length of light reaching the detectors. Because the spectral resolution depends on the optical path length, the out-of-plane leakage limits the resolution.

Engineering disorder to increase sensitivity

To reduce the out-of-plane scattering, we note that it occurs when the scattering from the disordered media reduces the magnitude of the in-plane propagation constant $k_{\|}$ of the light such that it is no longer confined outside the light cone ($|k_{\|}| > \omega/c$, where ω is the angular frequency and c is the speed of light). As the light index-guided in the silicon layer undergoes scattering, the in-plane propagation constant changes as $k'_{\|} = k_{\|} + \mathbf{q}$, where $k'_{\|}$ is the new in-plane propagation constant and $\mathbf{q}$ is the spatial vector of the scattering medium. As long as $|k'_{\|}| > \omega/c$, the scattered light remains

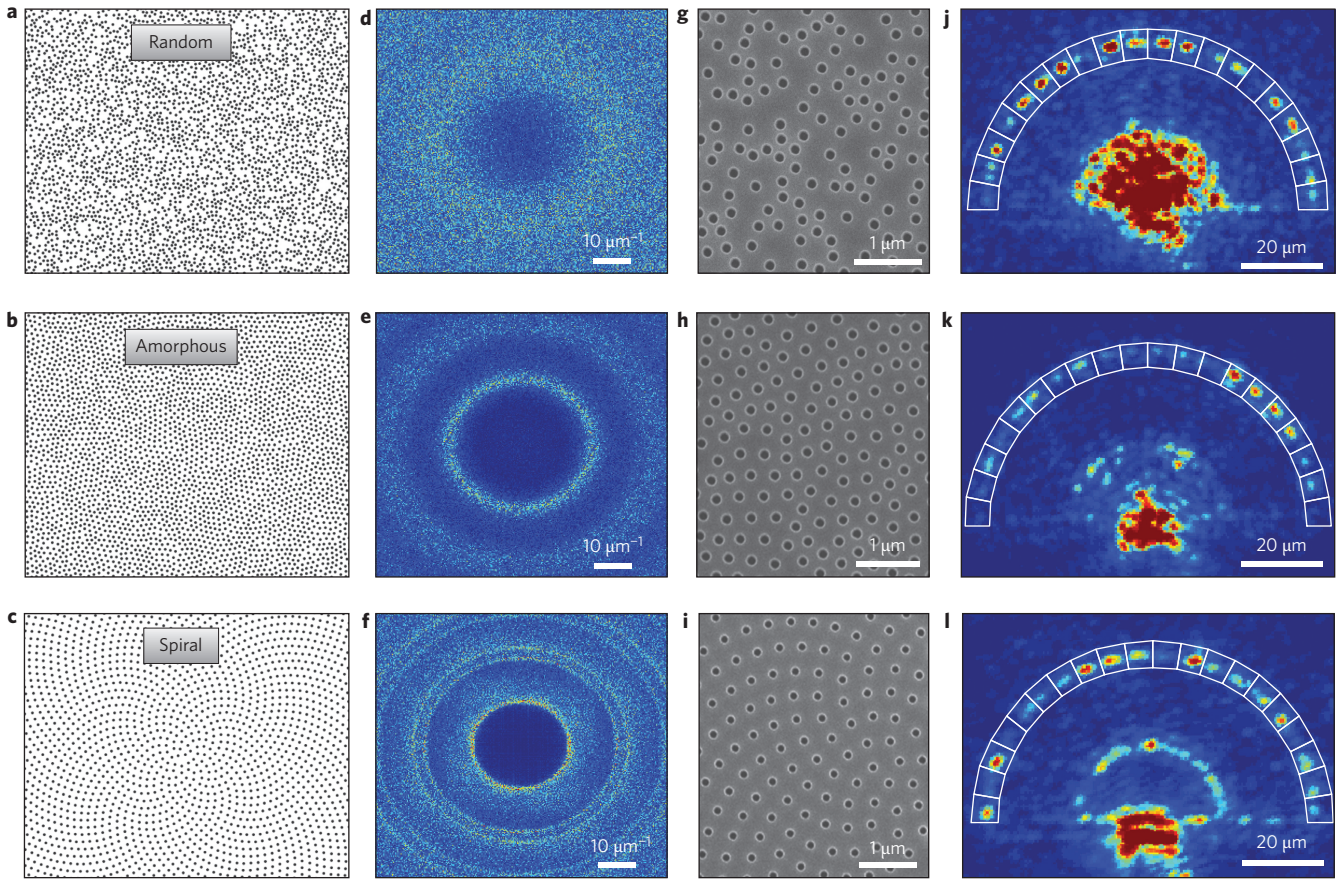

Figure 3 | Amorphous and spiral spectrometers with reduced out-of-plane leakage. a–i, Real space patterns (**a–c**), two-dimensional Fourier spectra (**d–f**) and SEM images (**g–i**) of the random structure, photonic amorphous structure and golden-angle spiral lattice used for on-chip spectrometers. The random structure has all spatial vectors, but the amorphous and spiral structures have dominant spatial vectors represented by the bright circles due to structural correlations. **j–l**, Optical near-field images of the three spectrometers. The input wavelength is set at $\lambda = 1{,}500$ nm. The intensity of light scattered out of plane is dramatically reduced in the amorphous and spiral structures.

outside the light cone. However, if $|k'_{\parallel}| < \omega/c$, the scattered light can leak out of the silicon layer into the air, reducing the collection efficiency of the spectrometer. By engineering the disorder, we can control the spatial vectors present in the scattering medium and influence the available $\mathbf{q}$ to reduce out-of-plane scattering.

We therefore sought to replace the completely random structure with partially random ones by introducing structural correlations. In particular, we considered two alternative scattering media: a photonic amorphous structure and a golden-angle spiral lattice. The former (Fig. 3b) has short-range order[22–24], as there is a characteristic spacing of adjacent scatterers—air holes[25]. The latter (Fig. 3c) is a deterministic aperiodic structure[26,27], which has been used to describe the arrangement of seeds in sunflower heads to ensure the most even distribution of seeds without clumping. We calculated the spatial Fourier transform of these two patterns to compare with a random pattern. The amplitude of the spatial Fourier spectra, plotted in Fig. 3d–f, represents the likelihood of finding a spatial vector $\mathbf{q}$. The random structure has all possible spatial vectors, and its Fourier spectrum is continuous. The photonic amorphous structure and the golden-angle spiral lattice, in contrast, exhibit bright circles, indicating the existence of dominant spatial vectors. If these vectors have large enough amplitudes, most scattering events will keep the light outside the light cone. Hence, by adjusting the characteristic spacing of air holes, we can lower the probability of out-of-plane scattering.

We designed the amorphous and spiral structures to act as the dispersive element in the spectrometer. To operate at a wavelength of ~1,500 nm, the average spacing of air holes was chosen to be 343 nm, and the radius of the air holes was 75 nm. For comparison, we also made a random structure with the same size and density of air holes. To estimate the out-of-plane scattering loss, we performed numerical simulations for all three scattering media. The full three-dimensional simulations are computationally heavy, so we calculated the fields in two dimensions using an effective index of refraction for the silicon layer (Supplementary Section S6). We considered the TE polarized light with in-plane electric fields, and performed a two-dimensional Fourier transform of the fields to obtain the wavevectors of light propagating inside the system. We then computed the fraction of wavevectors within the light cone so as to estimate the relative strength of out-of-plane scattering for the random, amorphous and spiral structures[27]. Experimentally there are two light cones, one for air above the silicon layer and the other for silica underneath ($|k_{\parallel}| > n_s\omega/c$, where $n_s = 1.5$ is the refractive index of silica). Because the latter is larger than the former, we used it in the computation, and found the light in the random medium had 38% and 81% more energy inside the light cone than the amorphous and spiral structures, respectively (Supplementary Section S6). These results confirmed our expectation that the structural correlations can be used to reduce out-of-plane scattering.

Finally, we fabricated a set of spectrometers with all three scattering media to perform an experimental comparison. SEM images of the three scattering media are shown in Fig. 3g–i. We monitored the out-of-plane scattering by imaging the scattered light from above the sample. As seen in Fig. 3j, significant out-of-plane scattering

is observed from the random structure. However, Fig. 3k,l shows the out-of-plane scattering loss is significantly reduced in the photonic amorphous structure and the golden-angle spiral lattice. This observation confirms that adding structural correlation to the scattering medium can reduce the insertion loss and improve the collection efficiency of the spectrometer. For a quantitative comparison, we estimated the transmission for the three spectrometers, by dividing the sum of the intensities of all detectors by the intensity of the scattered light at the entrance of the spectrometer. The transmission was measured in the wavelength range 1,500–1,525 nm with a 0.25 nm step, and then averaged. The amorphous and spiral structures exhibited 2.85 and 2.77 times higher transmission than the random structure, respectively. In addition to reducing the out-of-plane scattering, the amorphous and spiral spectrometers maintained similar spectral resolution and bandwidth to the random spectrometer (Supplementary Section S7).

Conclusion

In summary, we have shown that multiple scattering in a disordered photonic structure can be used for a compact chip-based spectrometer. The enhanced optical path length afforded by multiple scattering enables high resolution to be achieved with a small footprint. A photonic-crystal boundary was used to confine the light in the disordered medium and channel it to the detectors. The input spectra were accurately reconstructed from the spatial intensity distributions of transmitted light. We achieved 0.75 nm resolution with 25 nm bandwidth around the wavelength of 1,500 nm with a semicircular random structure with a radius of 25 μm. Finally, we engineered the disorder to reduce the out-of-plane scattering loss. By replacing the completely random structure with a photonic amorphous structure or a golden-angle spiral lattice, we were able to control the spatial vectors available for out-of-plane scattering. This work may lead to a new approach to building miniature spectrometers for applications such as lab-on-a-chip spectroscopy.

Methods

The spectrometers were fabricated on SOI wafers with a 220 nm silicon layer on top of a 3 μm SiO_2 layer. The random structure, photonic-crystal boundary and the coupling waveguides were all defined during a single electron-beam lithography exposure. The pattern was then transferred to the silicon layer via reactive ion etching in a chlorine environment. The scattering media (random, amorphous and spiral) consisted of 75-nm-radius air cylinders. The photonic-crystal boundaries were designed to support a full bandgap for TE polarized light in the wavelength range of operation of 1,500–1,525 nm. They were formed from triangular arrays of 180-nm-radius air holes with a lattice constant of 505 nm. The spectrometer was tested using a tunable, near-infrared laser (HP 8168F), which was coupled to a single-mode, polarization-maintaining lensed fibre. The lensed fibre delivered the laser beam to the ridge waveguide at the cleaved edge of the chip. The tunable laser was used to calibrate the spectrometer transmission matrix and then to test the ability of the spectrometer to reconstruct various probe spectra. The device was tested under TE polarization (electric field in the plane of the wafer). Scattered light was imaged from above the chip using a ×50 objective (NA = 0.55) and an InGaAs camera (Xenics Xeva 1.7-320). The random spectrometer also works for TM polarized light provided that the transmission matrix for the TM polarization is calibrated.

Received 28 March 2013; accepted 26 June 2013; published online 28 July 2013

References

1. Janz, S. *et al.* Planar waveguide Echelle gratings in silica-on-silicon. *IEEE Photon. Technol. Lett.* **16,** 503–505 (2004).
2. He, J. *et al.* Monolithic integrated wavelength demultiplexer based on a waveguide Rowland circle grating in InGaAsP/InP. *J. Lightwave Technol.* **16,** 631–638 (1998).
3. Zirngibl, M., Dragone, C. & Joyner, C. H. Demonstration of a 15×15 arrayed waveguide multiplexer on InP. *IEEE Photon. Technol. Lett.* **4,** 1250–1253 (1992).
4. Zirngibl, M., Dragone, C. & Joyner, C. H. Fabrication of 64 × 64 arrayed-waveguide grating multiplexer on silicon. *Electron. Lett.* **31,** 184 (1995).
5. Fukazawa, T., Ohno, F. & Baba, T. Very compact arrayed-waveguide-grating demultiplexer using Si photonic wire waveguides. *Jpn J. Appl. Phys.* **43,** L673–L675 (2004).
6. Cheben, P. *et al.* A high-resolution silicon-on-insulator arrayed waveguide grating microspectrometer with sub-micrometer aperture waveguides. *Opt. Express* **15,** 2299–2306 (2007).
7. Mossberg, T. W. Planar holographic optical processing devices. *Opt. Lett.* **26,** 414–416 (2001).
8. Babin, S. *et al.* Digital optical spectrometer-on-chip. *Appl. Phys. Lett.* **95,** 041105 (2009).
9. Peroz, C. *et al.* Multiband wavelength demultiplexer based on digital planar holography for on-chip spectroscopy applications. *Opt. Lett.* **37,** 695–697 (2012).
10. Momeni, B., Hosseini, E. S., Askari, M., Soltani, M. & Adibi, A. Integrated photonic crystal spectrometers for sensing applications. *Opt. Commun.* **282,** 3168–3171 (2009).
11. Little, B. E. *et al.* Ultra-compact Si–SiO_2 microring resonator. *IEEE Photon. Technol. Lett.* **10,** 549–551 (1998).
12. Nitkowski, A., Chen, L. & Lipson, M. Cavity-enhanced on-chip absorption spectroscopy using microring resonators. *Opt. Express* **16,** 11930–11936 (2008).
13. Kyotoku, B. B. C., Chen, L. & Lipson, M. Sub-nm resolution cavity enhanced micro-spectrometer. *Opt. Express* **18,** 102–107 (2010).
14. Xia, Z. *et al.* High resolution on-chip spectroscopy based on miniaturized microdonut resonators. *Opt. Express* **19,** 12356–12364 (2011).
15. Sharkawy, A, Shi, S. & Prather, D. W. Multichannel wavelength division multiplexing with photonic crystals. *Appl. Opt.* **40,** 2247–2252 (2001).
16. Xu, Z. *et al.* Multimodal multiplex spectroscopy using photonic crystals. *Opt. Express* **11,** 2126–2133 (2003).
17. Kohlgraf-Owens, T. W. & Dogariu, A. Transmission matrices of random media: means for spectral polarimetric measurements. *Opt. Lett.* **35,** 2236–2238 (2010).
18. Hang, Q., Ung, B., Syed, I., Guo, N. & Skorobogatiy, M. Photonic bandgap fiber bundle spectrometer. *Appl. Opt.* **49,** 4791–4800 (2010).
19. Redding, B. & Cao, H. Using a multimode fiber as a high-resolution, low-loss spectrometer. *Opt. Lett.* **37,** 3384–3386 (2012).
20. Redding, B., Popoff, S. M. & Cao, H. All-fiber spectrometer based on speckle pattern reconstruction. *Opt. Express* **21,** 6584–6600 (2013).
21. Pine, D. J., Weitz, D. A., Chaikin, P. M. & Herbolzheimer, E. Diffusing-wave spectroscopy. *Phys. Rev. Lett.* **60,** 1134–1137 (1988).
22. Edagawa, K., Kanoko, S. & Notomi, M. Photonic amorphous diamond structure with a 3D photonic band gap. *Phys. Rev. Lett.* **100,** 013901 (2008).
23. Rechtsman, M. *et al.* Amorphous photonic lattices: band gaps, effective mass, and suppressed transport. *Phys. Rev. Lett.* **106,** 193904 (2011).
24. Cao H. & Noh, H. in *Amorphous Nanophotonics* (eds. Rockstuhl, C. & Scharf, T.) 227–265 (Springer, 2013).
25. Yang, J-K. *et al.* Photonic-band-gap effects in two-dimensional polycrystalline and amorphous structures. *Phys. Rev. A* **82,** 053838 (2010).
26. Dal Negro, L. & Boriskina, S. V. Deterministic aperiodic nanostructures for photonics and plasmonics applications. *Laser Photon. Rev.* **6,** 178–218 (2011).
27. Vardeny, Z. V., Nahata, A. & Agrawal, A. Optics of photonic quasicrystals. *Nature Photon.* **7,** 177–187 (2013).

Acknowledgements

The authors thank A. Dogariu, M. Fink, A. Mosk, A. Yamilov, S. Gigan and S. Popoff for useful discussions. This work was supported by the National Science Foundation (NSF; grants nos. DMR-1205307 and ECCS-1128542). Computational resources were provided under the Extreme Science and Engineering Discovery Environment (XSEDE; grant no. DMR-100030). Facilities use was supported by YINQE and NSF MRSEC DMR-1119826.

Author contributions

H.C. and B.R. designed the spectrometers. B.R. fabricated the spectrometers and carried out all the testing and spectrum reconstruction. S.F.L. performed the FDFD simulation of spectrometers and R.S. helped B.R. characterize the spectral correlation of speckle patterns in random media. B.R. and H.C. prepared the manuscript with input from S.F.L.

Additional information

Supplementary information is available in the online version of the paper. Reprints and permissions information is available online at www.nature.com/reprints. Correspondence and requests for materials should be addressed to H.C.

Competing financial interests

The authors declare no competing financial interests.